Ocean Engineering 167 (2018) 142–155

Contents lists available at ScienceDirect

Ocean Engineering

journal homepage: www.elsevier.com/locate/oceaneng

Wake characteristics of stationary catenary risers with different incoming flow directions

Hongbo Zhu[a], Dai Zhou[a,b,c,*], Yan Bao[a,**], Rui Wang[a], Jiabao Lu[a], Dixia Fan[d], Zhaolong Han[a,b]

[a] School of Naval Architecture, Ocean and Civil Engineering, Shanghai Jiao Tong University, 800 Dongchuan Road, Shanghai, 200240, PR China
[b] State Key Laboratory of Ocean Engineering, Shanghai Jiao Tong University, 800 Dongchuan Road, Shanghai, 200240, PR China
[c] Collaborative Innovation Center for Advanced Ship and Deep-Sea Exploration(CISSE), Shanghai, 200240, PR China
[d] Department of Mechanical Engineering, MIT, Cambridge, MA, 02139, USA

ARTICLE INFO

Keywords:
Catenary riser
Wake topology
Hydro-forces
Vortex shedding frequency
Spectral/*hp* element method

ABSTRACT

In this paper, we numerically investigate three-dimensional flow past a freely hanging stationary riser in catenary shape (referred to CR) with the angle of incoming flow direction with respect to the plane aligned with the CR ranging from $\alpha = 0° \sim 90°$ at a low Reynolds number of 100. The flow dynamics are governed by the incompressible Navier-Stokes equations and a high-order spectral/*hp* element method is employed for the solutions of the flow field. The numerical results present that the wake topology behind the CR is strongly influenced by the incoming flow direction. In particular, in the range of small angle of incoming flow direction ($0° \lesssim \alpha \lesssim 40°$), the wake is completely suppressed; in the medium range of $40° \lesssim \alpha \lesssim 50°$, vortex shedding is developed firstly at the top side of the concave part, and then gradually spread over the span towards the convex part; wake instability is developed sufficiently along the whole span when the flow incidence is over 50°. The wake dynamics is further explored by examining the temporal evolution of hydro-forces and field quantities along the span and their frequency characteristics. It is revealed that the mechanism of axial flow that is varied along the span of CR can explain hydro-dynamics of the wake behavior of the CR.

1. Introduction

Highly flexible risers, such as steel catenary risers, are widely deployed for deep-water drilling industry to convey oil from the seabed to the sea surface, since it can offer a low cost alternative to conventionally used rigid risers on floating platforms and can also provide economic riser design solutions for fixed platforms. For such type of risers, it is commonly practical to incorporate a buoyant portion on an intermediate section of the riser or an upward force at a point via a buoy. This leads the riser in standard configurations of lazy wave, steep-wave, lazy-S and steep-S, as shown in Fig. 1, according to whether the riser rests along the sea bed and the means by which the buoyancy is achieved by (Yong and Qiang, 2005).

In terms of simplest modeling, a freely hanging configuration can be considered as a catenary riser (CR). In contrast to conventional straight riser, the angle of the axis of catenary geometry with respect to incoming flow direction varies along the curved span and it has great influence on the surrounding flow behavior. This can be expected from a few studies on flow past a deformed body that were carried out recently taking into account of the inclination effect on the wake dynamics (Miliou et al., 2003, 2007; Gallardo et al., 2011, 2013, 2014). Considering as a prototype of CR (Miliou et al., 2003, 2007), studied the wake structures behind a curved cylinder whose centerline is a quarter section of a ring. Their investigation showed that there were two completely different phenomena when the flow was applied onto the convex-shaped model and the concave-shaped model. In the convex configuration case, a fully three-dimensional vortex shedding was observed at $Re = 100$ and $Re = 500$. For the concave configuration, the vortex shedding was completely suppressed at $Re = 100$, but at $Re = 500$ the wake is energized with vortex shedding in particular at the top side of the riser (Gallardo et al., 2011, 2013, 2014). numerically investigated the turbulent wake of the same configuration but in the turbulent regime ($Re = 3900$). It was found that the turbulent wake structures behind the upper side of the convex configuration were more coherent due to the periodic shedding of primary vortices.

The geometry of catenary shape can be divided into convex part and

* Corresponding author. School of Naval Architecture, Ocean and Civil Engineering, Shanghai Jiao Tong University, 800 Dongchuan Road, Shanghai, 200240, PR China.
** Corresponding author.
E-mail addresses: zhoudai@sjtu.edu.cn (D. Zhou), ybao@sjtu.edu.cn (Y. Bao).

https://doi.org/10.1016/j.oceaneng.2018.05.030
Received 6 June 2017; Received in revised form 9 May 2018; Accepted 14 May 2018
Available online 31 August 2018
0029-8018/

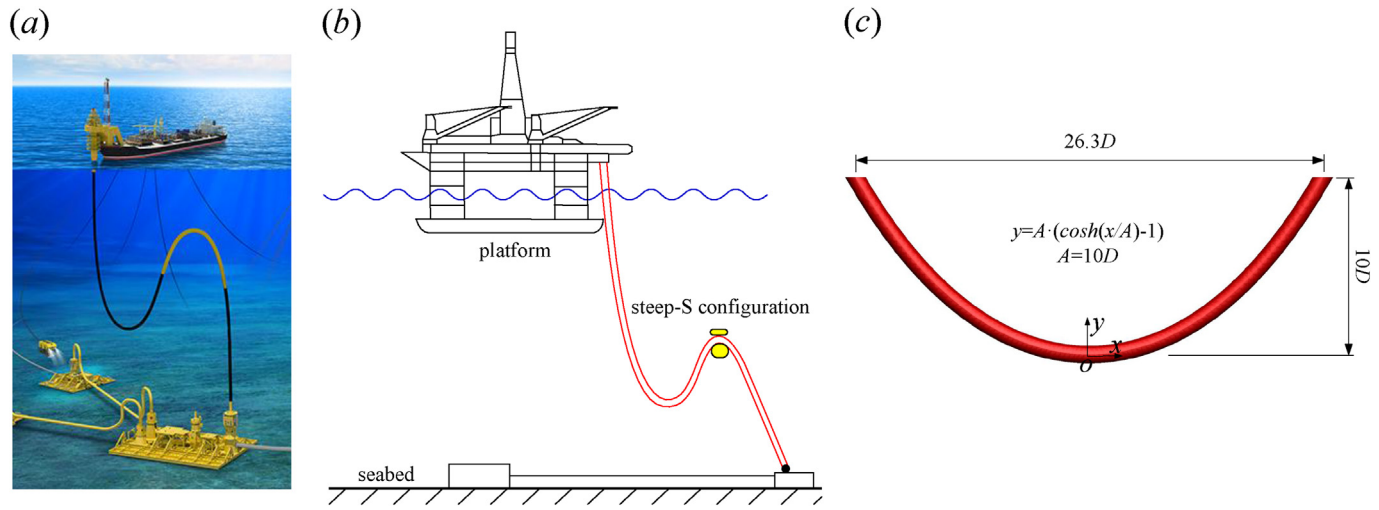

Fig. 1. Problem set up: (*a*) practical engineering application; (*b*) sketch of the steep-S riser; (*c*) basic geometry model in this investigation. *D* is the non-dimensional diameter of the riser.

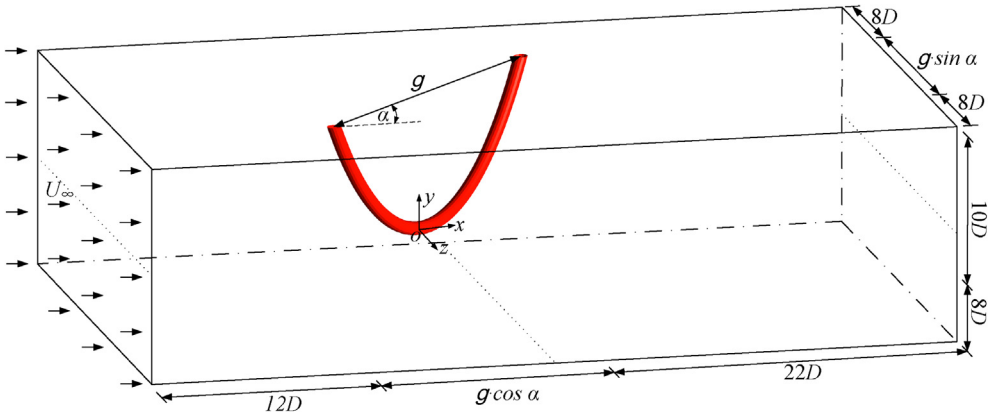

Fig. 2. Sketch of the catenary riser in a computational domain; the inclination of the riser is scaled by the angle between the incoming flow direction and the plane associated with the axial line of the riser.

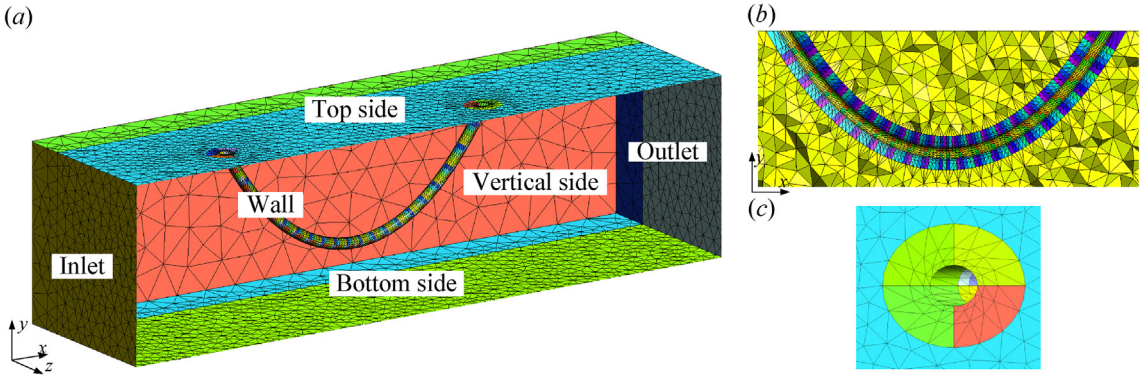

Fig. 3. Mesh topology around the CR for the case of $\alpha = 0°$: (*a*) three-dimensional view; (*b*) the central (x, y)-plane; (*c*) close view around the wall.

concave part, regarding the flow direction, and they may produce profound interference effect in their corresponding wake. Flow interference effect has been investigated deeply for the wake of the flow past multi-cylinders in proximity (Sumner et al., 2000; Hu and Zhou, 2008a; Bao et al., 2011). (Sumner et al., 2000) identified as many as nine wake patterns on the basis of FV (flow visualization) and PIV (particle image velocimetry) techniques in their experimental investigation of the flow around two staggered circular cylinders (Hu and Zhou, 2008a, 2008b). also characterized four distinct flow structures experimentally from the wake evolution of two-staggered circular cylinders at $Re = 7000$ (Sumner et al., 2008). presented the correlation between the Strouhal number and the spacing of two staggered circular cylinders. A number of numerical simulations including of both two- and three-dimensional are also dedicated for the fundamental classification of wake patterns (Mittal et al., 1997; Akbari and Price, 2005; Thapa et al., 2015).

Generation of axial flow along the span is another key characteristic for the flow around catenary riser. Early attempts to explore the associated mechanism of axial flow was made on the wake of yawed

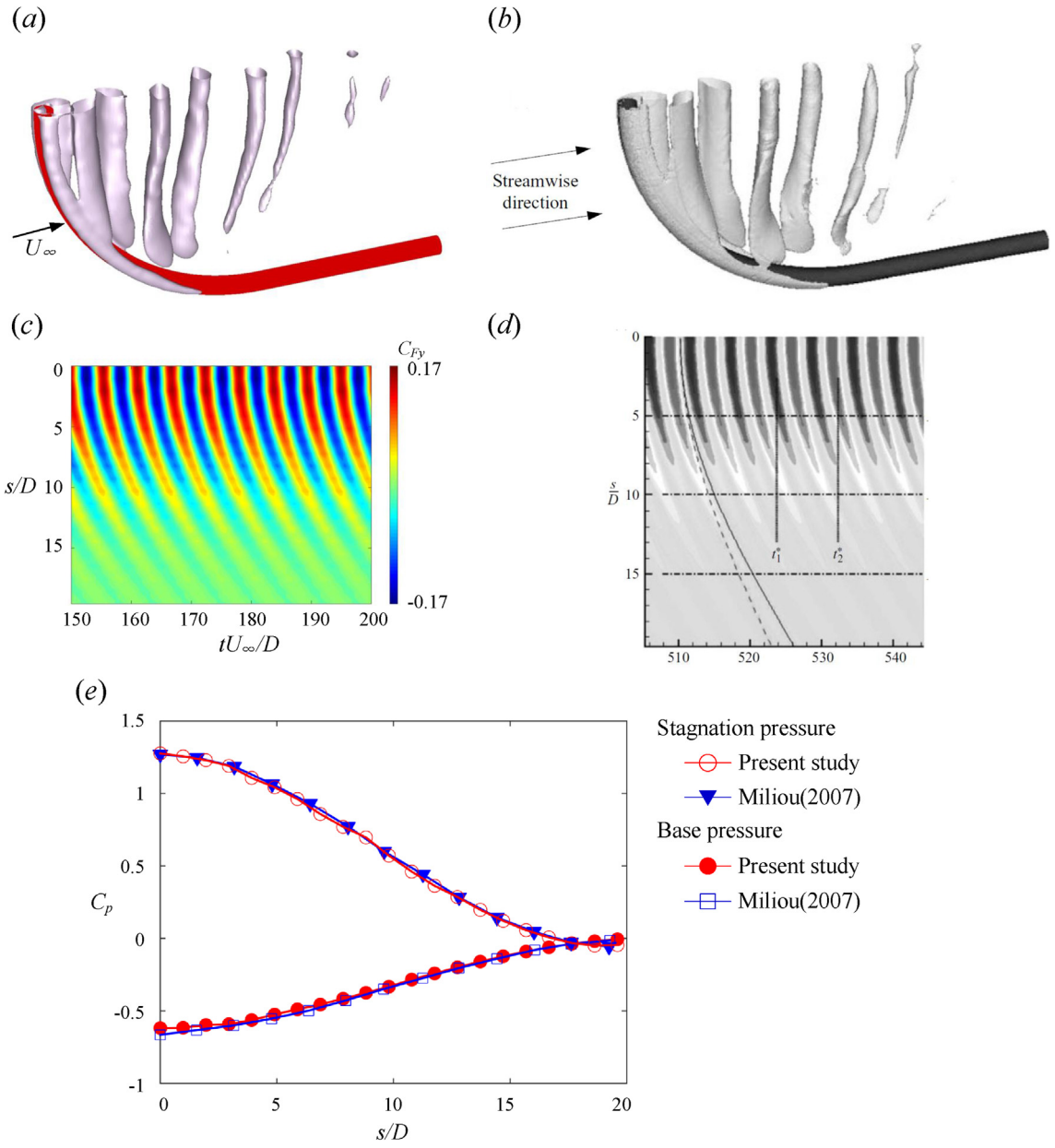

Fig. 4. Results of the validation test at $Re = 100$: (*a*) three-dimensional view of the wake topology, and vortex cores visualized by the vortex identification *Q*-criterion: iso-surfaces of the *Q*-value = 0.1; (*b*) vortex cores -(20, *c*) variation of sectional C_{Fy} along the length of the deformed circular cylinder, the isocontours range from –0.17 to +0.17; (*d*) variation of sectional C_{Fy} -(20, *e*) comparison of the time-averaged pressure along the length of the cylinder.

Table 1
Mesh resolution test at $\alpha = 90°$ ($P = 4$).

	Number of elements	C_{Fxmean}	C_{Fymean}	C_{Fzmean}
Mesh i	86627	4.6477 (0.883%)	−0.3281 (5.770%)	0
Mesh ii	105617	4.6068 (0.004%)	−0.3096 (0.193%)	0
Mesh iii	152992	4.6070	−0.3102	0

cylinders (Hanson, 1966). noted that the yaw angle has an effect on the laminar vortex shedding and the critical Reynolds number at which vortex shedding initiates (Hogan and Hall, 2010, 2011). studied the pressure fluctuations of circular cylinders for yawed angles ranging from 60° to 90° at high Reynolds number from 2.81×10^4 to 5.61×10^4. They found that the mean flow incidence caused the vortex shedding to become more disorderly and less spanwise coherent. The experimental results of two tandem circular cylinders (with a yawed downstream cylinder) indicated that the wake behind the cylinders behaved as a single large body when the local spacing ratios is small (Wilkins et al., 2013). With increasing of the local spacing ratios, some small-scale vortices were formed in the gap between the cylinders. At the largest local spacing, the shedding frequencies were no longer affected by each other (Younis et al., 2016). further investigated the flow past two non-parallel tandem cylinders and identified three distinct shedding patterns, which were namely of alternating reattachment flow regime, bi-stable flow regime and co-shedding flow regime.

Numerical study on the flow past yawed cylinder was conducted in low Reynolds number regimes (Zhao et al., 2009). investigated flow past a yawed cylinder of infinite length with yaw angles ranging from 0° to 60° at $Re = 1000$ by using direct numerical simulation (DNS) approach. They reported that the mean drag coefficient agreed well with the independence principle (IP) (Lam et al., 2012). simulated flow over two tandem yawed and unyawed wavy cylinders at a subcritical Reynolds number of 3900. They found that significant beneficial effect on

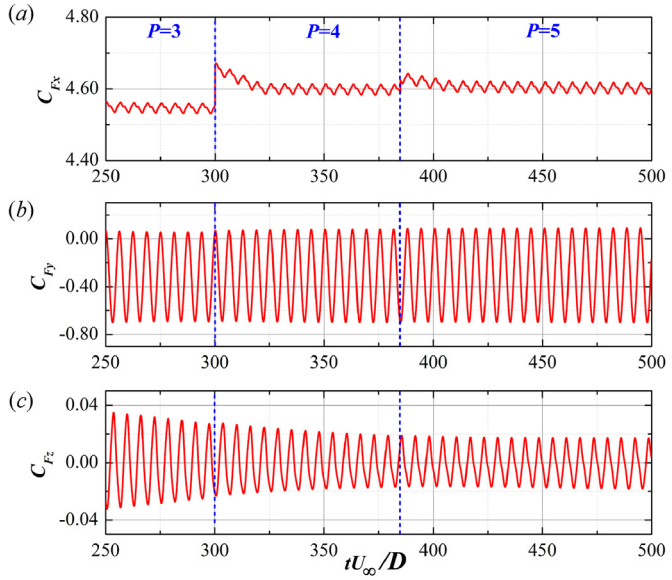

Fig. 5. Time history curve of the integrated forced coefficients in three Cartesian directions for the case of $\alpha = 90°$ at $Re = 100$.

Table 2
Spectral resolution test at $\alpha = 90°$ (Mesh ii).

	C_{Fxmean}	C_{Fymean}	C_{Fzmean}
$P = 3$	4.5739 (0.707%)	−0.3156 (1.708%)	0
$P = 4$	4.6068 (0.007%)	−0.3096 (0.226%)	0
$P = 5$	4.6065	−0.3103	0

fluctuating force suppression and drag reduction can be achieved at spacing ratios ranging of 1.5 ~ 5.5 (Zhao et al., 2013). examined numerically the flow transition in the wake of a circular cylinder at two incidence angles of 0° and 45°. It was found that the RMS (root mean square) of the lift coefficient at $\alpha = 45°$ is about 20%–25% larger than that at $\alpha = 0°$ at the Reynolds number ranged from 250 to 500.

The geometry of a curved body in catenary shape is much more complicated when compared with the yawed straight cylinder. In this situation, not only the axial flow is generated along the span of the CR, but also the flow interference involves the wake dynamics. In this paper, we investigate the wake characteristics of flow around a stationary long riser, whose geometry is shaped with a generalized catenary equation. Direct numerical simulation by employing high-order spectral/*hp* method is carried out for the solution of the incompressible flow in laminar flow regime at low Reynolds number of 100. The main objective is to explore how does the angle between the approaching flow and the plane aligned with the curved catenary riser influence the essential features of vortex formation and shedding and further hydrodynamic characteristics of catenary riser. Apart from the interest from the view of fundamental physics, this work can be considered as the first step for study of flexible risers that undergo vortex-induced vibrations under the effect of ocean streams and waves.

2. Physical model and numerical methodology

2.1. Physical model

The geometric configuration of the CR with circular cross section of diameter D whose axial line is described by the catenary equation in Cartesian coordinates as follows:

$$y = A(cosh(x/A) - 1) \tag{1}$$

where, A is the catenary coefficient, $A = 10D$ in this investigation. x, y denote the incoming flow direction and the vertical direction, respectively. The non-dimensional height of CR is fixed at $h/D = 10$, while the distance between the two end points is fixed at $g = 26.3D$ (g is the maximum centre-to-centre spacing of the CR). In this investigation, the inclination angle, α, which is defined as the angle between the incoming flow direction and the plane determined by the curved axial line of the CR, is varied in the range of 0° ~ 90°. This means that the CR is aligned with the flow direction at $\alpha = 0°$, while it is perpendicular to the flow direction at $\alpha = 90°$. The time dependent flow is described by the incompressible Naiver-Stokes equations and the continuity equation as:

$$\frac{\partial \mathbf{u}}{\partial t} + \mathbf{u}\cdot\nabla\mathbf{u} = -\nabla p + \frac{1}{Re}\nabla^2\mathbf{u} \tag{2}$$

$$\nabla\cdot\mathbf{u} = 0 \tag{3}$$

where $\mathbf{u}$ is the velocity field, p is the pressure, $Re = U_\infty D/\nu$ is the Reynolds number based on the free-stream velocity U_∞, ν is the kinematic viscosity of fluid and D is the diameter of the CR.

2.2. Numerical methods

Computations have been performed using a high-order spectral/*hp* element time stepping code-Nektar++ (Karniadakis and Sherwin, 2013; Cantwell et al., 2015). The spatial domain is discretized into tetrahedral finite elements and within each macro-element, the high-order Lagrange polynomials associated with Gauss-Lobatto-Legendre (GLL) interpolation points are employed as shape and weighting functions, which could improve the computational efficiency. The temporal discretization, on the other hand, is based on a high-order stiffly stable splitting scheme which allows the primitive variables to be treated independently over each time step (Miliou et al., 2003). The details on the algorithm can refer to (Karniadakis and Sherwin, 2013) and (Karniadakis et al., 1991), which are shown in briefly as follows:

Firstly, calculate a first intermediate velocity field ($\tilde{\mathbf{u}}$) evaluating the advection term explicitly and combining it with the solution at previous time-steps:

$$\frac{\tilde{\mathbf{u}} - \sum_{q=0}^{J-1}\frac{\alpha_q}{\gamma_0}\mathbf{u}^{n-q}}{\Delta t} = \sum_{q=0}^{J-1}\frac{\beta_q}{\gamma_0}[-(\mathbf{u}\cdot\nabla)\mathbf{u}]^{n-q} \tag{4}$$

where γ_0, α_q, and β_q are the stiffly stable time integration coefficients which are given by (Karniadakis et al., 1991). J is the order of the time integration for the explicit terms ($J = 2$ in this work). Δt is the time step.

Secondly, solve a Poisson equation to obtain the pressure solution at the new time level with a high-order boundary conditions:

$$\Delta p^{n+1} = \left(\frac{\gamma_0}{\Delta t}\right)\nabla\cdot\tilde{\mathbf{u}} \tag{5}$$

Then, a second intermediate velocity field ($\tilde{\tilde{\mathbf{u}}}$) are calculated by:

$$\tilde{\tilde{\mathbf{u}}} - \tilde{\mathbf{u}} = -\left(\frac{\Delta t}{\gamma_0}\right)\nabla p^{n+1} \tag{6}$$

Finally, obtain the velocity field at the new time level by using the second intermediate velocity field as a forcing term in a Helmholtz equation:

$$\left(\Delta - \frac{\gamma_0}{\Delta t\nu}\right)\mathbf{u}^{n+1} = -\left(\frac{\gamma_0}{\Delta t\nu}\right)\tilde{\tilde{\mathbf{u}}} \tag{7}$$

The computational domain is a rectangular box that extends 22D downstream and 12D in upstream of the CR, 18D in the vertical direction and 10D both sides of the cross flow direction, as shown in Fig. 2. The mesh is comprised of tetrahedral elements for the domain discretization. The number of tetrahedral element is varied between 84928 ($\alpha = 0°$) and 105617 ($\alpha = 90°$) depending on α and the mesh in the near wake region of the CR is finely resolved. The perspective and cross-

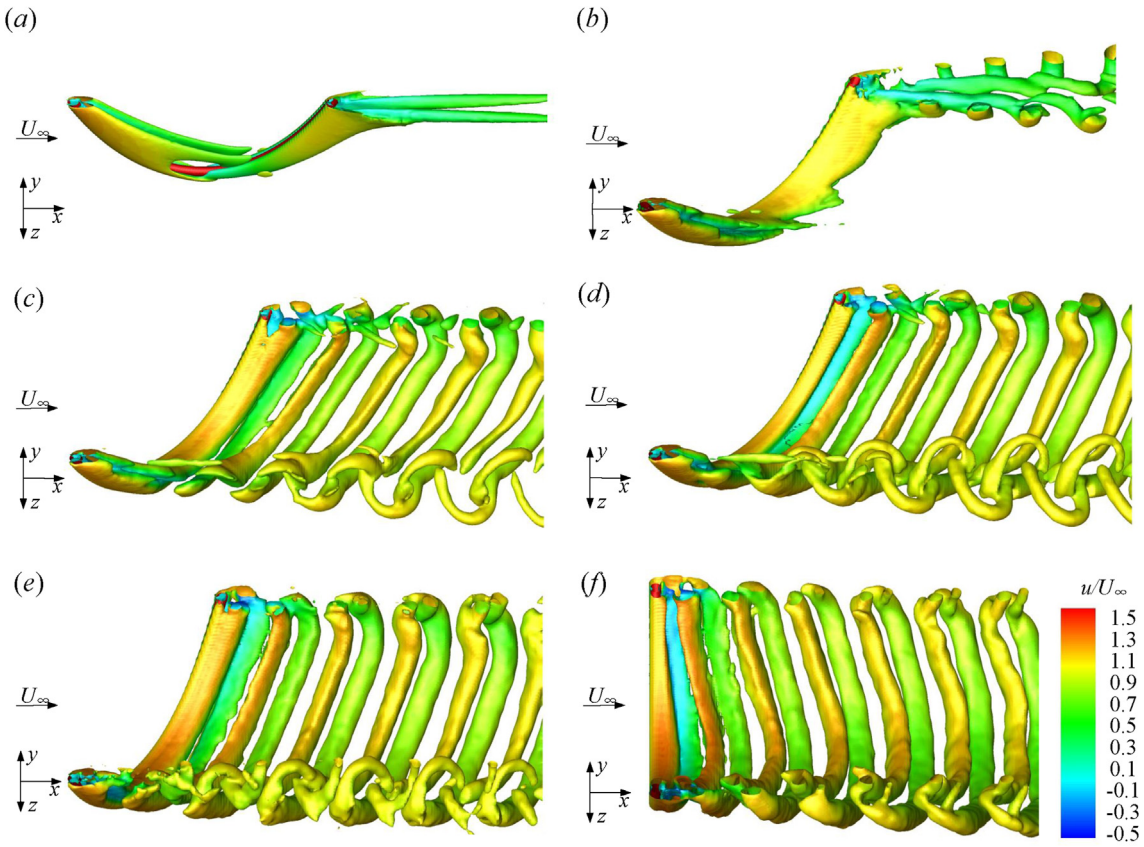

Fig. 6. Perspective view of the instantaneous wake topology for flow past a catenary riser at different incoming flow incidence (structure visualized by the vortex identification Q-criterion: iso-surfaces of the Q-value = 0.01, and the color denotes the streamwise u-velocity) in the view from the top side at Re = 100: (a) $\alpha = 0°$; (b) $\alpha = 40°$; (c) $\alpha = 45°$; (d) $\alpha = 50°$; (e) $\alpha = 60°$; (f) $\alpha = 90°$. (For interpretation of the references to color in this figure legend, the reader is referred to the Web version of this article.)

sectional views of the mesh for the representative case of $\alpha = 0°$ are shown in Fig. 3. A suitable choice of boundary conditions is essential for the numerical simulation. For the cases studied, the imposed boundary conditions are listed as follows:

1) A uniform velocity profile is specified to the inlet boundary:

$$U_\infty = 1, \quad v = 0, \quad w = 0 \tag{8}$$

2) The non-slip condition is applied at the wall of the CR:

$$u = 0, \quad v = 0, \quad w = 0 \tag{9}$$

3) The Neumann boundary condition is imposed at the outlet as:

$$\frac{\partial u}{\partial x} = 0, \quad \frac{\partial v}{\partial x} = 0, \quad \frac{\partial w}{\partial x} = 0 \tag{10}$$

4) The symmetry boundary condition is specified on the vertical sides:

$$u = 1, \quad v = 0, \quad w = 0 \tag{11}$$

5) Finally, the top boundary condition is assigned as:

$$\frac{\partial u}{\partial y} = 0, \quad v = 0, \quad \frac{\partial w}{\partial y} = 0 \tag{12}$$

Besides, the pressure was set to zero ($p = 0$). This can gives a fully developed zero stress condition in order to avoid reflections from the outlet.

2.3. Validation test

A validation test is conducted at Re = 100 for which the geometry configuration of convex shape is the same with that of (Miliou et al., 2007). The 3D wake developed in the flow is visualized by Q-criterion (De Villiers, 2007). As shown in Fig. 4(a) and (b), the vortex cores in the near wake are bent according to the curvature of the cylinder, but start to distort further downstream, showing the same features when compared to the results of (Miliou et al., 2007). Fig. 4(c) depicts the variation of sectional lift coefficient (C_{Fy}) along the non-dimensional length (s/D) of the curved cylinder. It is also noticed that the profile of C_{Fy} is in good agreement with the data given by (Miliou et al., 2007), see Fig. 4(c) and d. The time-averaged variations of pressure (C_p) along the stagnation line as well as the base line are compared against the results reported in (Miliou et al., 2007). Two results collapse well in the same curve lines, as depicted in Fig. 4(e). This then verifies the implementation of spectral/hp element method for the solution of wake flows of curved cylinder and the polynomial order of $P = 4$ is sufficient for the accuracy of the solution of flow at this low Reynolds number.

2.4. Grid independence

As mentioned in subsection 2.3, the polynomial order of $P = 4$ is sufficient for the accuracy of the solution of flow at this low Reynolds number. However, in order to further ensure the accuracy of the numerical results, as well as the computational efficiency, the grid sensitivity analyses are performed by varying the resolution and the polynomial order (P = 3–5) for case of $\alpha = 90°$, Re = 100, in which the wake flow is much energetic.

Table 1 summarizes the results from different meshes for the fixed

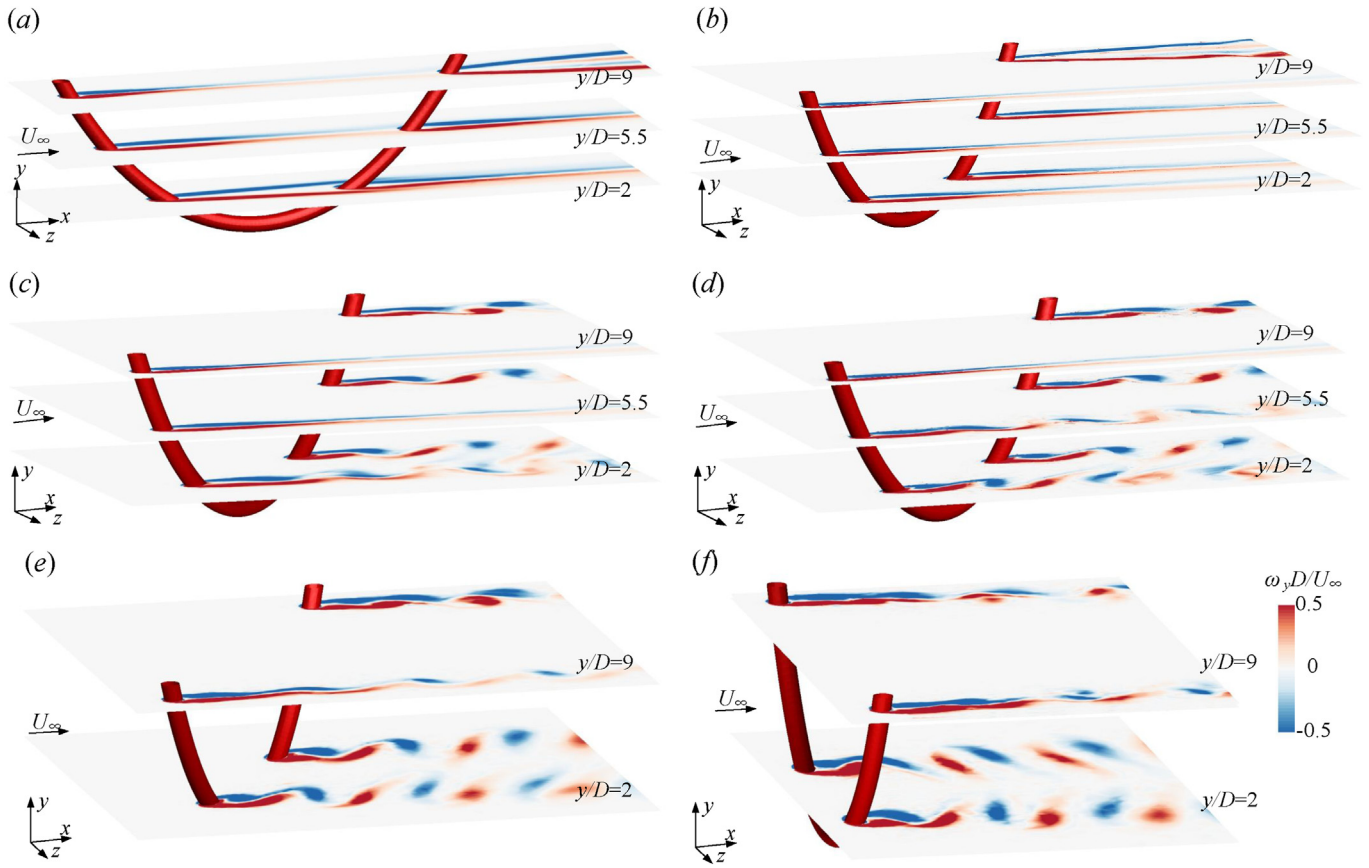

Fig. 7. Contours of vorticity components in the vertical direction (ω_y) at different slices along the span of the CR: (*a*) $\alpha = 0°$; (*b*) $\alpha = 40°$; (*c*) $\alpha = 45°$; (*d*) $\alpha = 50°$; (*e*) $\alpha = 60°$; (*f*) $\alpha = 90°$.

polynomial order of $P = 4$, with Mesh iii being the reference. The maximum percentage change of C_{Fymean} is reduced from 5.770% to 0.193% while going from Mesh ii to Mesh iii. The value of P is also switched successively at $tU_\infty/D = 300$ and 385 for the medium mesh as shown in Fig. 5. Table 2 presents the time-averaged values of these global quantities. A discrepancy of only 0.226% in the magnitude of C_{Fy} is noticed when P changes from 4 to 5. Thereby, it can be concluded that the polynomial order of $P = 4$ with the medium ii is sufficient for the accuracy of the solution of flow at this laminar flow.

3. Numerical results and discussion

3.1. Wake topology

The wake topology and associated 3D vortical structures of the flow past a CR is visualized by *Q*-criterion in Fig. 6. At small angles of incidence, particularly in the range of $0° \lesssim \alpha \lesssim 40°$, the vortex-shedding from two half parts of CR are completely suppressed. Typically, Fig. 6(*a*) presents the perspective view of the vortical structures at $\alpha = 0°$, showing stabilized features of steady wake along the whole span of the CR. As shown in this figure, the wake becomes narrow at the top side of the gap region, whilst it becomes wide behind the concave part with formation of a swirling vortex pair in the streamwise direction. More importantly, the coherent structures aligned with the curved axis of the CR imply that axial flow has great impact on the wake dynamics of the CR. The mechanism associated with the wake suppression is essentially similar as that given by (Miliou et al., 2007). They suggested that the strong axial flow and the streamwise vorticity play a key role in suppressing of the wake dynamics. Similar wake regime can be retained until α over 40°. However, when $\alpha > 0°$ the wake region formed behind the CR is twisted along the length following the inclination of the plane associated with the axial line of the CR.

Fig. 6(*b*) shows the instantaneous wake topology at $\alpha = 40°$. Unlike the flow pattern for the smaller angles of incidence, the vortical structures behind the concave part indicates a weak oscillation in the wake flow particularly at the side close to the top boundary. This weak oscillation is represented by the formation of array of vortex tubes in vertical direction at the outer sides of the pair of vortex cores in streamwise direction. Clearly, in this situation the swirling vortices in streamwise direction still dominate the wake at the top side of the downstream region. However, the appearance of vortical structures in vertical direction reveals that the growth of wake instability is started from the concave part of the CR. With the increasing of the angle between the incoming flow direction and the plane associated with the curved CR, the destabilized portion of the wake region, which is characterized by the alternating rolling of vortical structures into the wake, is further spread towards the convex part of the CR. It can be illustrated in Fig. 6(*c*) for the case of $\alpha = 45°$, showing that the alternating shedding vortex tubes formed in curved configuration starts from the top side of the concave part and terminates around the middle section of the convex part. As depicted in Fig. 6(*d*), for the case of $\alpha = 50°$, the region of vortex shedding further occupies the top side of the convex part.

As α further increases, the approaching flow tends to be perpendicular to the plane associated with the CR. Correspondingly, the wake behind the CR becomes more and more energized and unstable until it changes into complete vortex shedding regime along the whole span. Fig. 6(*e*) and (*f*) show the evolution of representative 3D vortical tubes for the fully developed vortex shedding regime at $\alpha = 60°$ and $\alpha = 90°$, respectively. As shown in these figures, the Kármán vortex street in curved shape is generated behind the CR and the associated vortex tubes terminate at the two top sides of the CR. The alternating

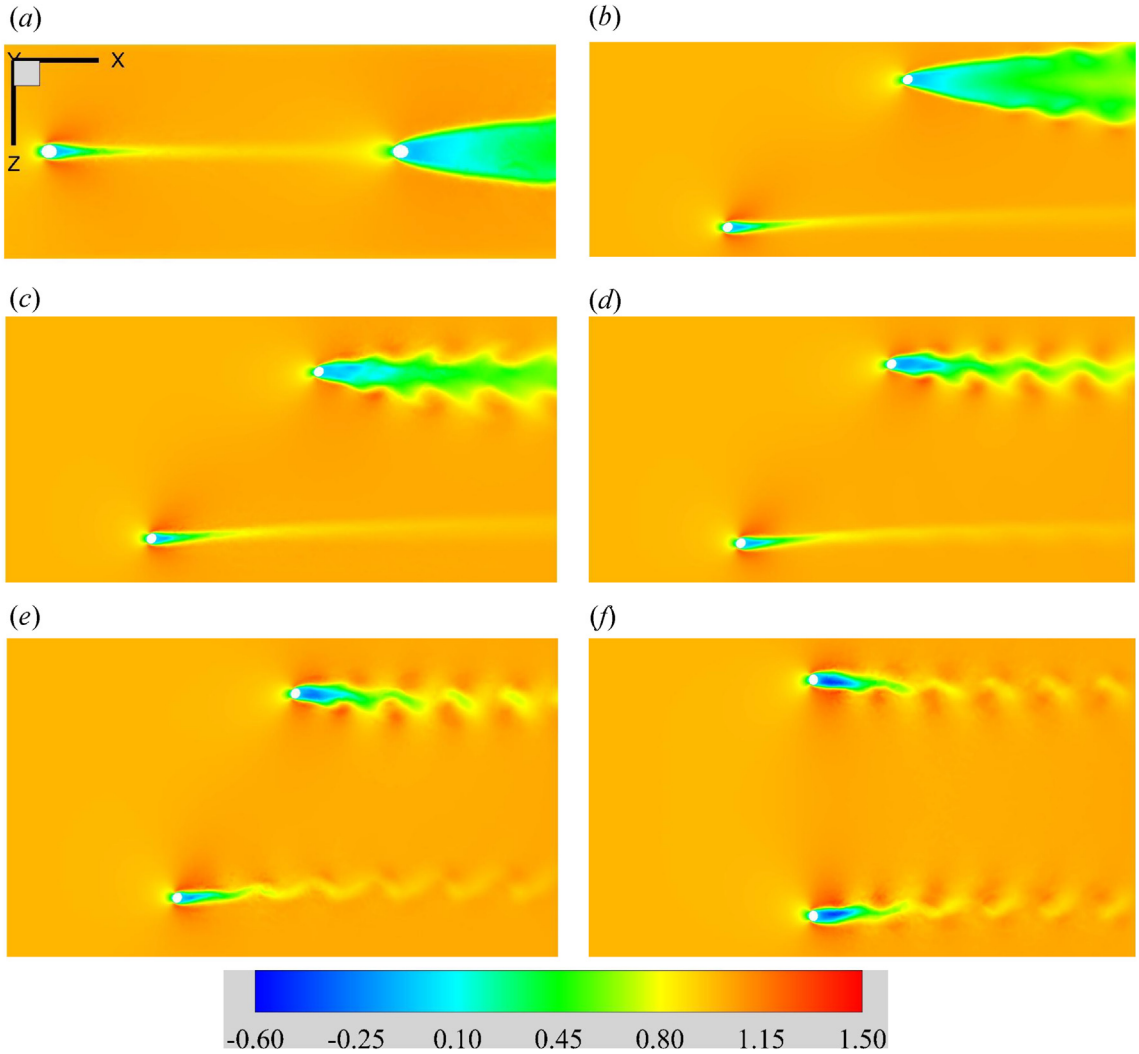

Fig. 8. u-velocity contours at $y = 10D$ on the x–z plane, $Re = 100$: (*a*) $\alpha = 0°$; (*b*) $\alpha = 40°$; (*c*) $\alpha = 45°$; (*d*) $\alpha = 50°$; (*e*) $\alpha = 60°$; (*f*) $\alpha = 90°$.

formation of vortex rollers at the two sides appear to be aligned with the plane associated with the CR for the both cases. However, for the front case, the wake intensity is not symmetrically distributed along the span, while it is the case for the aft case.

Further insight on the variation of wake features with the inclination angle can be shed from the evolution of the components of vorticities. Fig. 7 shows the contours of the vorticity component in vertical direction, ω_y, on the slices, which are distributed along the span of CR. The wake oscillation is also firstly detected in Fig. 7(*b*), and then it spreads along the span from the concave part to the convex part in Fig. 7(*c*) and (*d*) and finally occupies the whole span of the CR in Fig. 7 (*e*) and (*f*). In general, the change of wake behavior along the span presented in this figure is well consistent with that observed in wake topology in Q-criterion contours shown in Fig. 6.

For given positions along the span which are located symmetrically with respect to the mid-plane at $s/L = 0.5$, the corresponding local Reynolds numbers are identical; however, the wake structures presented in Fig. 6 indicate that the strength of wake is not symmetrically distributed with the mid-span except for the case at $\alpha = 90°$. This behavior will be further demonstrated in the spectral analysis in the following section. Thus, in the basis of the study of (Lucor and Karniadakis, 2003), it is confirmed that the independence principle (IP) is not valid for the catenary configuration of freely hanging riser considered in this work. In essence, the flow mechanism for this dynamics is due to the effects of axial flows that strongly depends on specific geometric configurations (for instance convex or concave) and flow direction.

To investigate the origin of instabilities, we explore how streamwise velocity is varied along the CR. Fig. 8 illustrates the u-velocity contours in the vicinity of the CR at $y = 10D$ on the x–z plane, indicating that wake instability is developed firstly at the top side of the concave part and then gradually spread over the span towards the convex part. A variation in the wake width along the span can also be observed. Additionally, it is noticed that the strength of recirculation region amplified with the increase of incoming flow incidence, especially at the top side of the concave part. Strong recirculation promotes absolute instability in the recirculation region, which is correlated with the wake instability originated at the top side of the concave part.

3.2. Sectional forces

The temporal evolution of sectional force distribution along the span of the CR is examined in this section. Fig. 9 presents the results of the three components of non-dimensionalized sectional forces including C_{Fx}, C_{Fy} and C_{Fz} for the cases of $\alpha = 0°$ and 30°. Equation (13) gives the integrated force coefficients of C_{Fx}, C_{Fy} and C_{Fz} in three coordinate directions x, y and z:

$$C_{Fx} = \frac{F_x}{\frac{1}{2}\rho U_\infty^2 S}, \quad C_{Fy} = \frac{F_y}{\frac{1}{2}\rho U_\infty^2 S}, \quad C_{Fz} = \frac{F_z}{\frac{1}{2}\rho U_\infty^2 S} \tag{13}$$

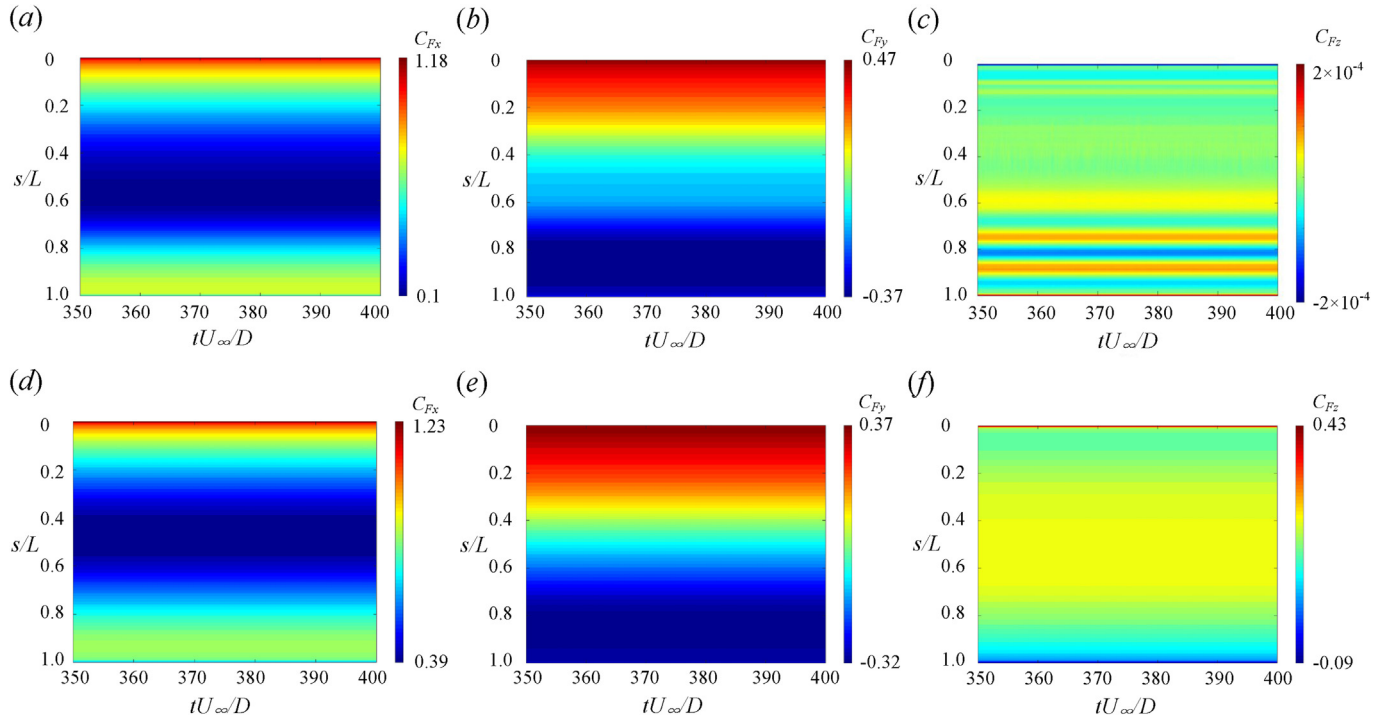

Fig. 9. Time evolution of sectional force components in different directions along the length of the CR for cases of $\alpha = 0°$ and 30°: ($a \sim c$) C_{Fx}, C_{Fy} and C_{Fz} for the case of $\alpha = 0°$; ($d \sim f$) C_{Fx}, C_{Fy} and C_{Fz} for the case of $\alpha = 30°$.

where ρ is the fluid density, F_x, F_y and F_z are the components of sectional force acting on the CR, and S is the characteristic area, i.e. is the projection area of the riser in the corresponding direction.

It can be clearly seen that there are no fluctuations in the forces for the both cases, which are consistent with the suppressed wake observed in the previous section. As shown in Fig. 9(a), C_{Fx} decreases along the length of the CR and reaches to the minimum value around the bottom side of the CR and then slightly increases again. C_{Fx} along the concave part of CR is much smaller when compared to the convex part. This behavior is caused by the flow interference effect from the tandem arrangement of the two half parts. In contrast, C_{Fy} decreases consistently along the span of the CR and obtains the minimum around the top side of the concave part. This is because the stagnation line is located at the lower side of the convex part and it switches onto the upper side of the concave part. Moreover, C_{Fz} is negligible along the whole span at $\alpha = 0°$, while its value increases significantly for the case of $\alpha = 30°$. The reason is that the frontal area of the CR increases with the increase of incoming flow incidence, therefore, the force in z-direction increases slightly as α increases.

The time variation of sectional force components along the span of the CR at $\alpha = 40°$, 45° and 50° are shown in Fig. 10. Nearly time-independent forces are observed in Fig. 10(a,b,c), which then imply that the strength of wake oscillation detected in the vortical structures behind the top side of the concave part is too weak (see Fig. 6(b)). However, it is intensified strongly for the cases of $\alpha = 45°$ and 50°, which are clearly verified by the visible fluctuation of C_{Fy} and C_{Fz}. It is also confirmed from the distribution of force fluctuations along the span that the wake oscillation is started from the concave part ($s/L > 0.5$) and then spread towards the convex part ($s/L < 0.5$). With the increasing of the inclination angle, the value of C_{Fx} within the bottom section increases significantly.

The components of sectional force along the span of CR at $\alpha = 60°$ and 90°, as typical instances for the fully developed vortex shedding regime, are depicted in Fig. 11. C_{Fx} reaches to a higher value in the range from 0.93 to 1.32 at $\alpha = 60°$ and from 1.13 to 1.39 at $\alpha = 90°$, which is larger than that obtained at smaller α. As compared with the case of $\alpha = 50°$ (Fig. 10(h)), the fluctuation in C_{Fy} is also further amplified when $\alpha = 60°$, as shown in Fig. 11(b). For the case of $\alpha = 90°$, the hydroforces along the span behaves symmetrically with respect to the mid-section ($s/L = 0.5$). The oscillation of C_{Fy} reaches the maximum at the mid-plane. It is also noticed that the peak-to-peak amplitude of C_{Fy} is ranged from -0.48 and 0.23 at the mid-plane ($s/L = 0.5$). The reason for the different magnitudes of crest and trough can be attributed to the unequal strength of shedding vortices generated at the two sides due to the curved configuration. Apparently, the fluctuation of C_{Fz} is maximized at the two inclined sides of the CR as shown in Fig. 11(f), whose peak-to-peak amplitude is ranged from -0.55 to 0.55.

3.3. Pressure along the axial line

Fig. 12 presents the pressure contours on the plane associated with the axial line of the CR. For the case of $\alpha = 0°$, the pressure contours shown in Fig. 13 (a) represents the distribution along the stagnation and base lines of the CR, since the incoming flow is parallel to the plane of the axial line. A positive value is detected both on the stagnation face of the convex and concave parts, while it changes into negative along the base line of the two parts. A significant variation of pressure contours is displayed as α increases. The pressure coefficients show consistently negative values along the whole span of CR, and their magnitude increases with the increase of α. Another interesting feature displayed in this figure is relevant to the generation of axial flow. It can be witnessed from the comparison of the different cases that the pressure gradient along the span is highly correlated to the inclination angle. The pressure gradient along the axial line is significant for the case of $\alpha = 0°$, while it is nearly negligible for the case of $\alpha = 90°$. More importantly, the decrease of magnitude of pressure gradient is also started from the concave part and then it spread over the span towards the convex part. This behaves highly consistent with the wake features discussed in the previous section. Therefore, it is then suggested that the variation of the axial flow along the span of CR is the prominent mechanism responsible for the variation of the wake dynamics along the span for different inclination angles.

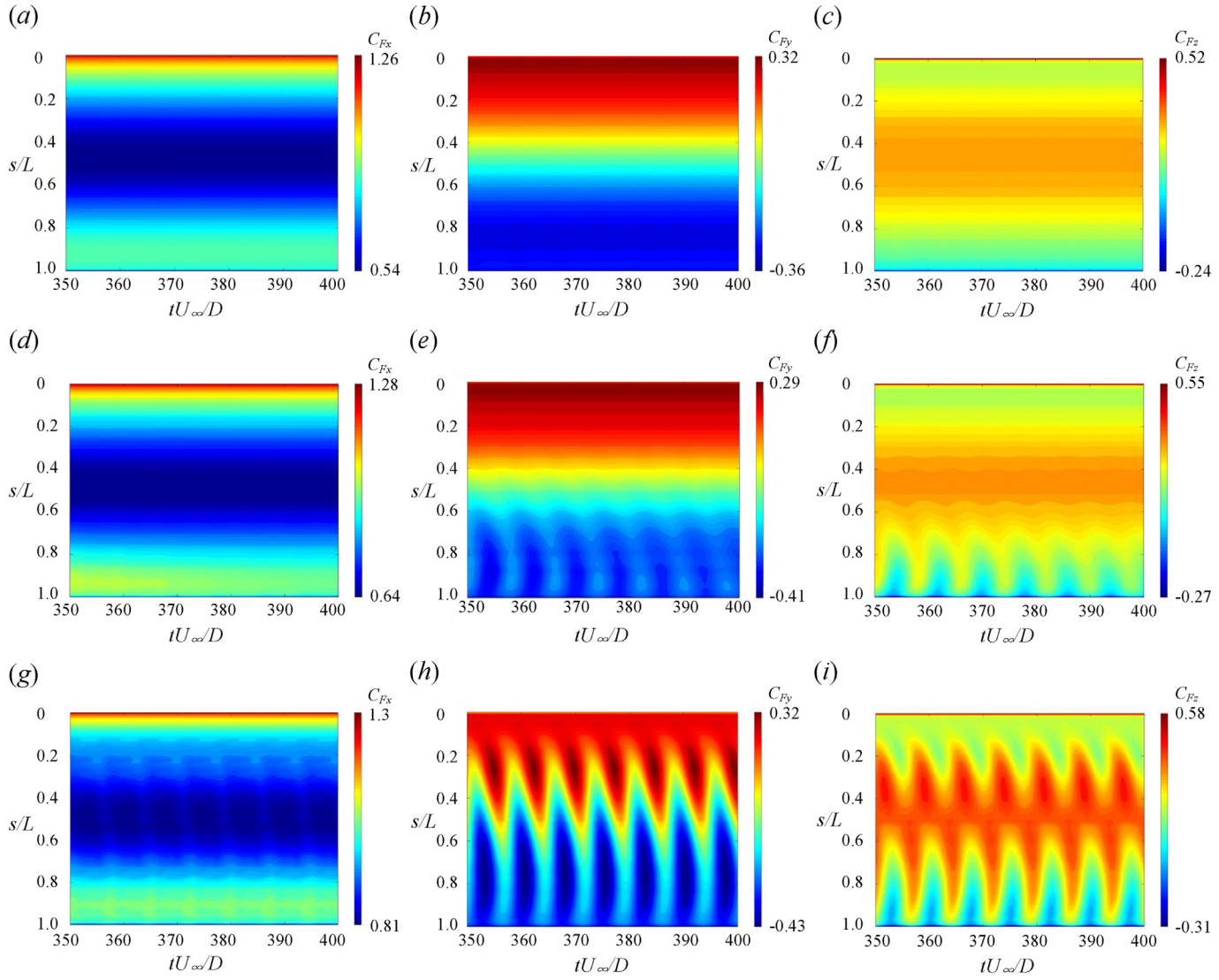

Fig. 10. Time evolution of sectional forces coefficient in different directions along the length of the CR for cases of $\alpha = 40°$, 45° and 50°: ($a \sim c$) C_{Fx}, C_{Fy} and C_{Fz} for case of $\alpha = 40°$; ($d \sim f$) C_{Fx}, C_{Fy} and C_{Fz} for case of $\alpha = 45°$; ($g \sim i$) C_{Fx}, C_{Fy} and C_{Fz} for case of $\alpha = 50°$.

3.4. Spectral analysis

The horizontal velocities are sampled along the span of CR and are used to investigate the frequency response characteristics of the wake using the power spectra density function, which is expressed by

$$\Phi(f) = \frac{\overline{\widetilde{w}(f)\widetilde{w}(f)^*}}{T} \tag{14}$$

where

$$\widetilde{w}(f) = \int_{-T/2}^{T/2} w(t) e^{-2\pi f t} dt \tag{15}$$

Φ is the power spectra. w is the horizontal velocity in z direction, T is the block length, f is the frequency and (*) represents the complex conjugate. The power spectral densities obtained at different locations along the span are shown in Figs. 13–16 respectively for $\alpha = 45° \sim 90°$.

When the CR is inclined at $\alpha = 45°$, there is a pronounced peak in the power spectra density, which is associated with the shedding frequency at $St = 0.130$, implying that the shedding wake of the CR is organized and associated with a dominant frequency. It is also noticed that the value of Φ varies along the spanwise location of the CR. The magnitude of the spectra on the concave part are several orders higher than those observed from the symmetric location of the convex part with respect to the mid plane. This observation also verifies that the wake oscillation at the concave part is much stronger when compared to the convex part, and their strength monotonically increases along the span of CR. Moreover, the second harmonics of shedding frequency, which is equal to 0.260, are also slightly discernible for this case as shown in Fig. 13.

As the inclination angle increases to the range of $\alpha = 50° \sim 60°$, the frequency components present different characteristics as shown in Figs. 14 and 15. For the cases at $\alpha = 50°$ and $\alpha = 60°$, the power spectral density have a dominant peak associated with the Strouhal number respectively of $St = 0.135$ and 0.147, higher than that for the case at $\alpha = 45°$. Higher harmonics are also excited in the power spectral density. The harmonic frequency components in the wake of multiple cylinders in close proximity were reported previously in the literature (Kiya et al., 1980; Sumner et al., 2000; Hu and Zhou, 2008a; Hu and Zhou, 2008b; bao et al., 2012). The peak associated with the second harmonic becomes comparable to the primary peak at the bottom side of the CR. The studies on the wake of multi-cylinders implies that the flow mechanism underlying the current frequency competence might be correlated to the flow interference effects between the adjacent parts of CR.

As shown in Fig. 16, when the angle of incidence increases to

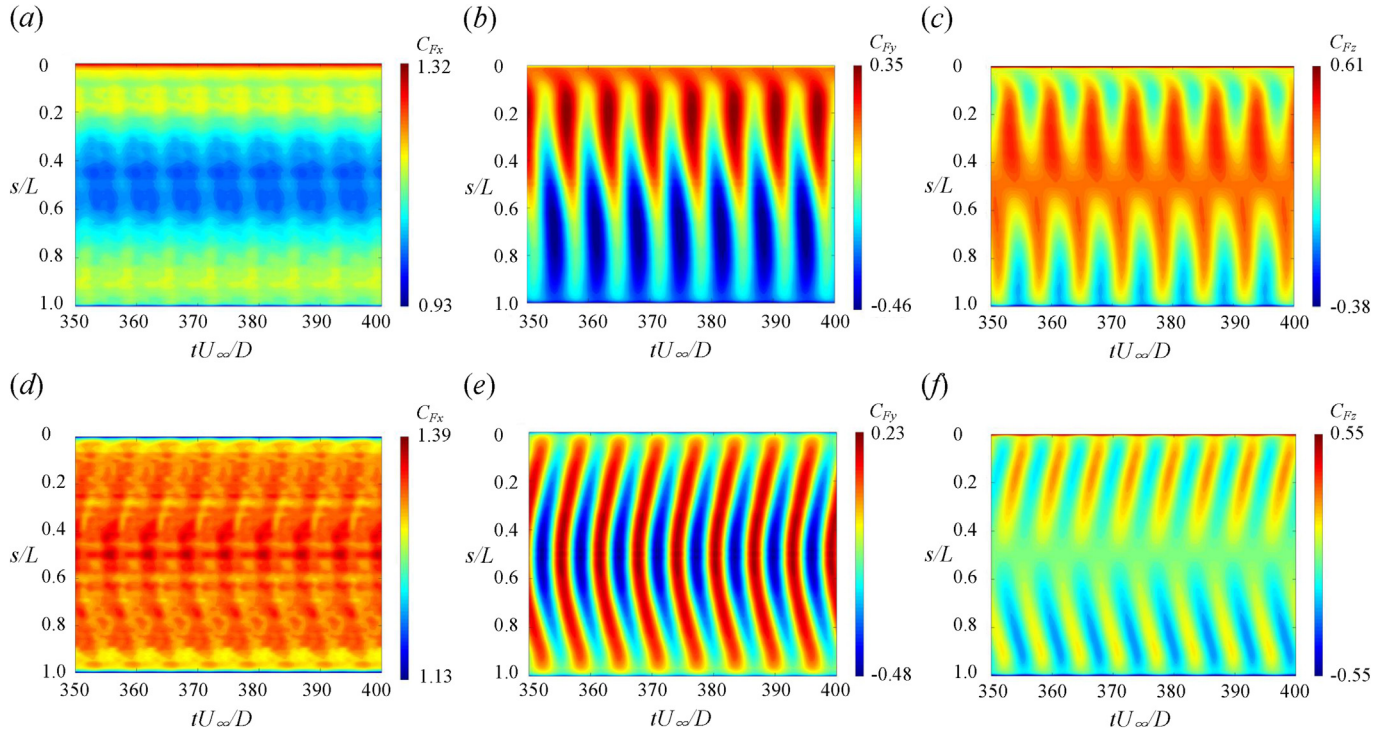

Fig. 11. Time evolution of sectional forces coefficient in different directions along the span of the CR for cases of $\alpha = 60°$ and 90°: ($a \sim c$) C_{Fx}, C_{Fy} and C_{Fz} for case of $\alpha = 60°$; ($d \sim f$) C_{Fx}, C_{Fy} and C_{Fz} for case of $\alpha = 90°$.

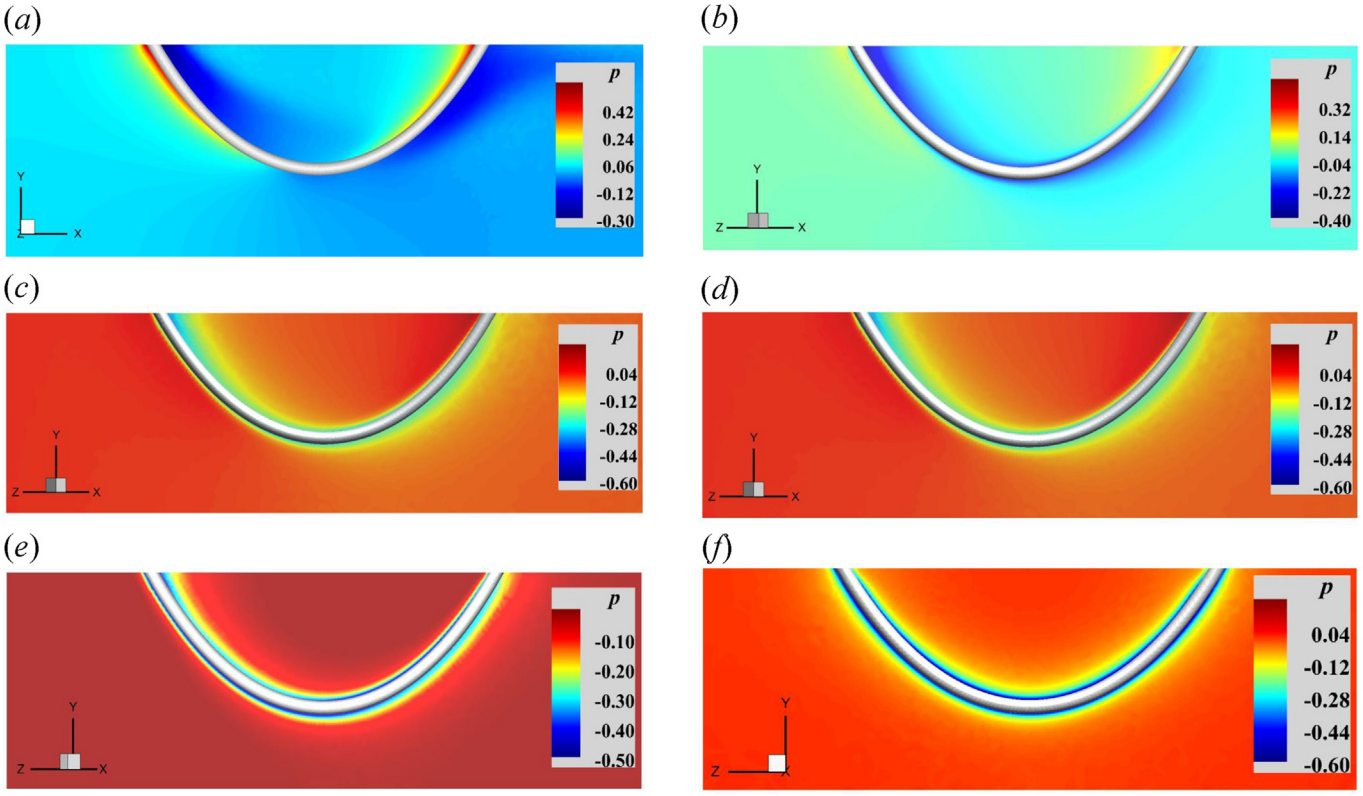

Fig. 12. The pressure contours on the surface aligned with the plane of curvature of the CR at $Re = 100$: (a) $\alpha = 0°$; (b) $\alpha = 40°$; (c) $\alpha = 45°$; (d) $\alpha = 50°$; (e) $\alpha = 60°$; (f) $\alpha = 90°$.

$\alpha = 90°$, the primary frequency corresponding to the vortex shedding period increases to a value as high as $St = 0.160$, which is very close to the shedding frequency of straight cylinder at the same Reynolds number (Williamson, 1996; Han et al., 2013). The wake is mainly dominated by the primary shedding frequency, which are much different from the previous cases, although multiple harmonics are still detected in the power spectral density, as depicted in Fig. 16. The variation of magnitude of the power spectral density for the dominant

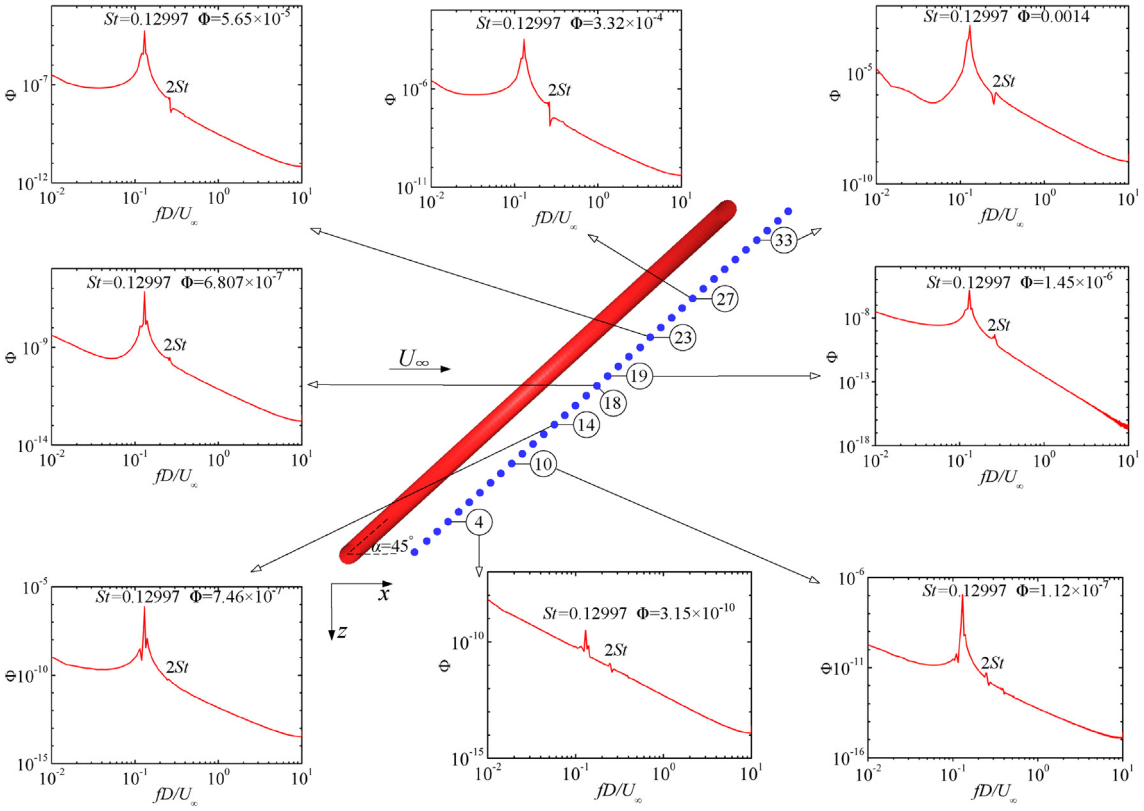

Fig. 13. Power spectra normalized by the velocity along the catenary riser span at different monitor points for the case of $\alpha = 45°$, view from the top.

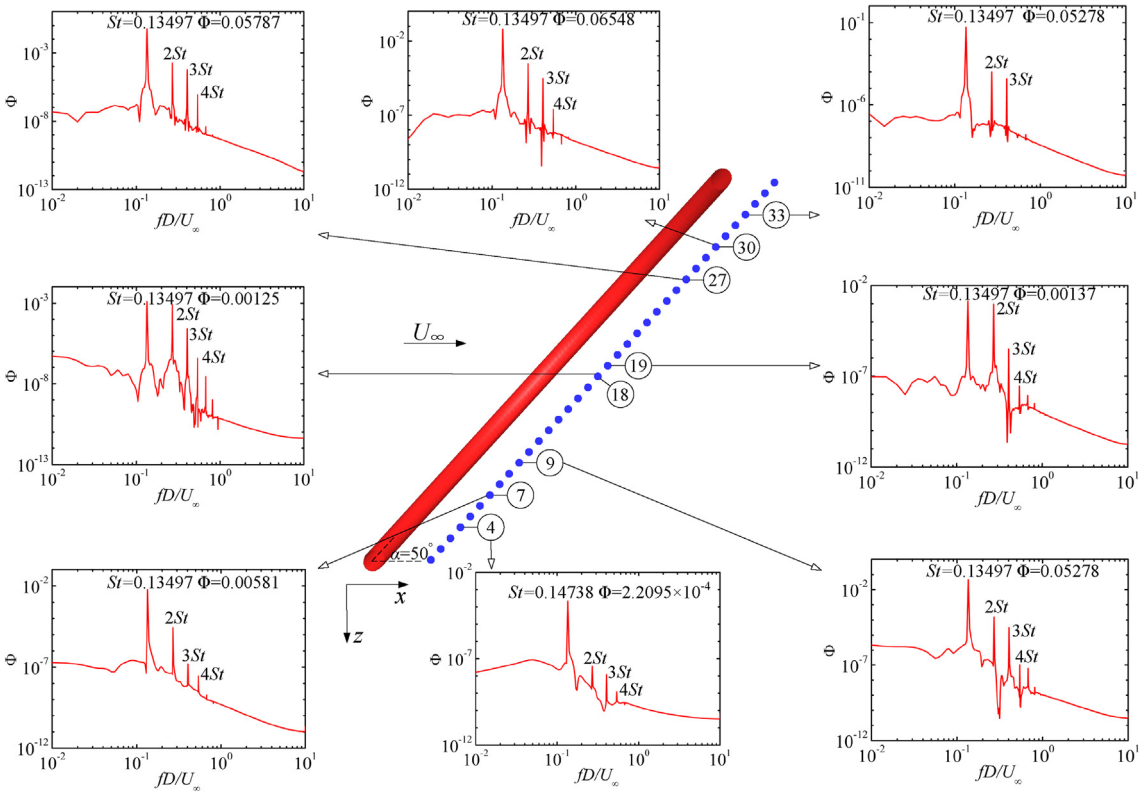

Fig. 14. Power spectra normalized by the velocity along the catenary riser span at different monitor points for the case of $\alpha = 50°$, view from the top.

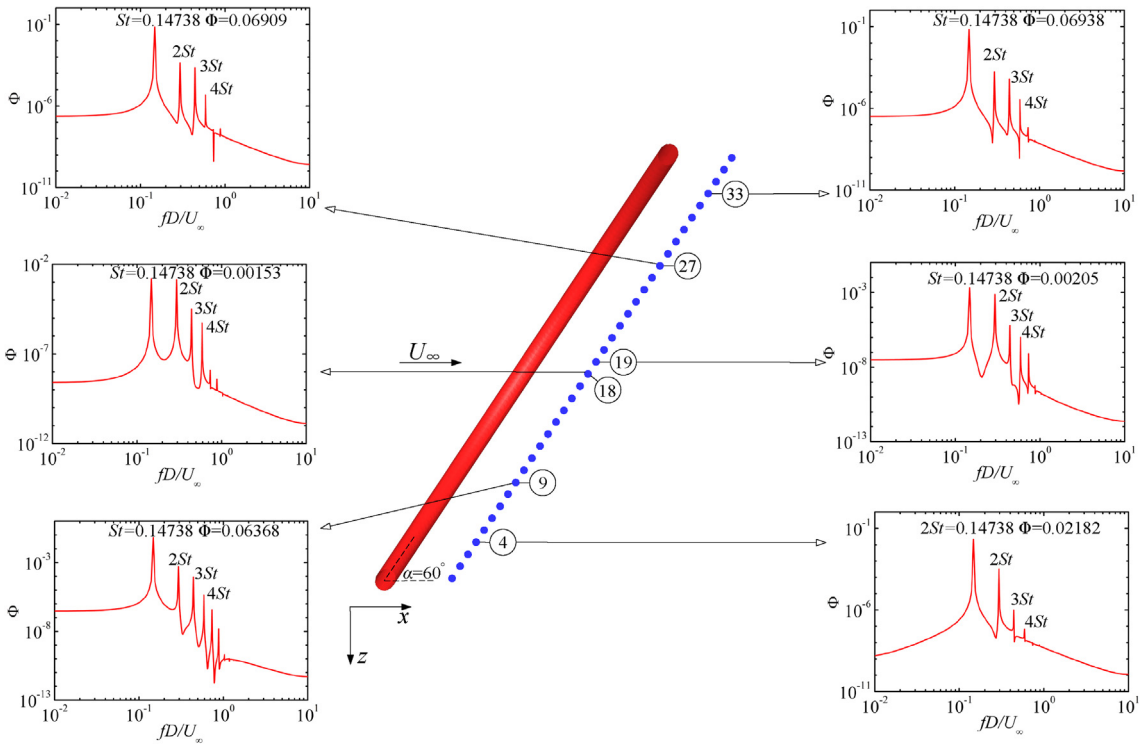

Fig. 15. Power spectra normalized by the velocity along the catenary riser span at different monitor points for the case of $\alpha = 60°$, view from the top.

frequency along the length of CR indicates that the strength of shedding vortices is minimized at the bottom side of the CR.

4. Conclusions

In this study, wake characteristics of three dimensional flow past a freely hanging stationary riser in catenary shape are investigated at a low Reynolds number of 100. The catenary configuration defined by equation (1) is inclined with the incoming flow direction, which is quantified by the angle between the incoming flow direction and the plane aligned with the curved axial line of the catenary riser. The flow dynamics are governed by the incompressible Navier-Stokes equations and a high-order spectral/*hp* element method is employed for their numerical solutions.

In the basis of the numerical results, the wake behind the catenary riser can be categorized into different regimes depending on the inclination angle with respect to the incoming flow. In the range of smaller incoming flow incidence ($0° \lesssim \alpha \lesssim 40°$), the wake is completely suppressed, showing stabilized features of steady wake along the whole span of the CR. As a consequence, the components of sectional force appear to be time-independent. Their distribution along the span of the CR is primarily correlated with the axial flow effect along the pan of the convex part and the concave part of CR.

As the flow incidence increases in the range of $40° \lesssim \alpha \lesssim 50°$, the wake is partially destabilized, which is started from the concave part and then gradually spread towards the convex part of catenary riser with increasing of incoming flow incidence. Correspondingly, the fluctuation of sectional force components especially in the vertical and crossflow directions is also detected in the concave part firstly and then develops in the same manner with the wake oscillation. With the increasing of the inclination angle, higher harmonics of frequency components and their influence become dominant in the unstable wake evolutions, as demonstrated in the power spectral analysis for the cases at $\alpha = 50°$ and 60°.

The vortex shedding wake is fully developed along the whole span of the CR when $\alpha \gtrsim 50°$, which is characterized by a formation of Kármán vortex street comprised of curved vortex tubes alternating shedding at the two sides of the catenary riser. The sectional force components therefore present oscillatory nature of the unstable wake along the whole span. With the further increase of inclinations, the shedding frequency is close to that of a straight cylinder at the same *Re*. At $\alpha = 90°$, the incoming flow is perpendicular with the plane of CR and both the wake topology and hydro-force distribution are symmetric with respect to the mid-plane at $s/L = 0.5$.

The pressure distribution along the span of CR reveals that the axial flow is greatly affected by the inclination angle. In specific, the corresponding pressure gradient varies along the span and it starts to decrease from the concave part and then spread to the convex part with the increasing inclination. Furthermore, this is the prominent mechanism for the variation of wake behavior of the CR for different inclinations.

A few recent studies revealed the effect of Reynolds number on the flow over a curved body (Miliou et al., 2007). studied the nature of flow past a curved cylinder both in laminar and transitional regimes corresponding to $Re = 100$ and $Re = 500$. More recently, a fully developed turbulent flow around a curved cylinder at $Re = 3900$ was numerically explored in (Gallardo et al., 2014). From the literature mentioned above, it is reasonable to expect that the wake features are also highly dependent on Reynolds number for the current geometry configuration. This is actually verified in a preliminary study conducted on the case of $\alpha = 0°$ at $Re = 500$. Vortex shedding with highly three-dimensionality was observed in the wake at $Re = 500$ (not shown here), whereas it is stabilized into a steady wake at $Re = 100$. In addition, the dynamic behaviors of wake were shown to be much complicated owing to the interactions between the convex and concave segments. For this reason, it is necessary to carry out further research on high Reynolds number flow. It is believed that this work will serve as a first step to further investigate the complicated wake in turbulent flow and even vortex-induced vibration of flexible risers of such complex configurations.

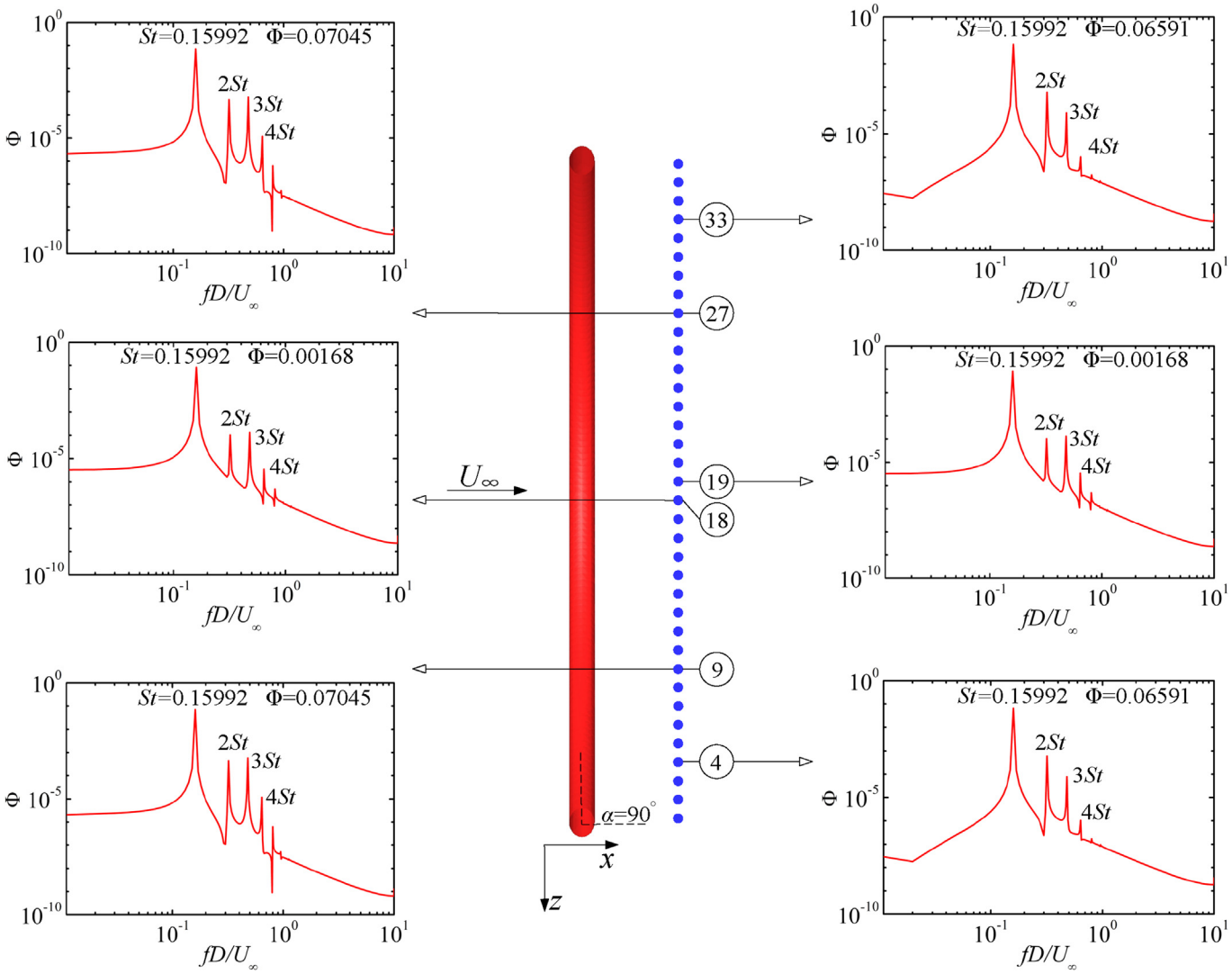

Fig. 16. Power spectra normalized by the velocity along the catenary riser span at different monitor points for the case of $\alpha = 90°$, view from the top.

Acknowledgments

The authors are grateful for the financial support from the National Natural Science Foundation of China (Nos. 11772193 and 51679139), the Major Program of the National Natural Science Foundation of China (No. 51490674), the Program for Professor of Special Appointment (Eastern Scholar) at Shanghai Institutions of Higher Learning, Shanghai Natural Science Foundation (No. 17ZR1415100 and 18ZR1418100). This work is also sponsored by Shanghai Pujiang Program (No. 17PJ1404300), Program for Intergovernmental International S&T Cooperation Projects of Shanghai Municipality (No. 18290710600), and New Enrolment Support of Shanghai Jiao Tong University (No. WF220401005). Computational support was also provided by the High Performance Computing Center (HPCC) at Shanghai Jiao Tong University.

References

Akbari, M., Price, S., 2005. Numerical investigation of flow patterns for staggered cylinder pairs in cross-flow. J. Fluid Struct. 20, 533–554.

bao, Y., huang, C., zhou, D., tu, J., han, Z., 2012. Two-degree-of-freedom flow-induced vibrations on isolated and tandem cylinders with varying natural frequency ratios. J. Fluid Struct. 35, 50–75.

Bao, Y., Zhou, D., Tu, J., 2011. Flow interference between a stationary cylinder and an elastically mounted cylinder arranged in proximity. J. Fluid Struct. 27, 1425–1446.

Cantwell, C.D., Moxey, D., Comerford, A., Bolis, A., Rocco, G., Mengaldo, G., De Grazia, D., Yakovlev, S., Lombard, J.-E., Ekelschot, D., et al., 2015. Nektar++: an open-source spectral/hp element framework. Comput. Phys. Commun. 192, 205–219.

De Villiers, E., 2007. The Potential of Large Eddy Simulation for the Modelling of wall Bounded Flows. PhD thesis. University of London.

Gallardo, J.P., Andersson, H.I., Pettersen, B., 2014. Turbulent wake behind a curved circular cylinder. J. Fluid Mech. 742, 192–229.

Gallardo, J.P., Pettersen, B., Andersson, H.I., 2011. Dynamics in the turbulent wake of a curved circular cylinder. J. Phys. Conf. 318, 062008 IOP Publishing.

Gallardo, J.P., Pettersen, B., Andersson, H.I., 2013. Effects of free-slip boundary conditions on the flow around a curved circular cylinder. Comput. Fluids 86, 389–394.

Han, Z., Zhou, D., Gui, X., Tu, J., 2013. Numerical study of flow past four square-arranged cylinders using spectral element method. Comput. Fluids 84, 100–112.

Hanson, A., 1966. Vortex shedding from yawed cylinders. AIAA J. 4, 738–740.

Hogan, J.D., Hall, J.W., 2010. The spanwise dependence of vortex-shedding from yawed circular cylinders. J. Pressure Vessel Technol. 132, 031301.

Hogan, J.D., Hall, J.W., 2011. Experimental study of pressure fluctuations from yawed circular cylinders. AIAA J. 49, 2349–2356.

Hu, J., Zhou, Y., 2008a. Flow structure behind two staggered circular cylinders. part 1. downstream evolution and classification. J. Fluid Mech. 607, 51–80.

Hu, J., Zhou, Y., 2008b. Flow structure behind two staggered circular cylinders. part 2. heat and momentum transport. J. Fluid Mech. 607, 81–107.

Karniadakis, G., Sherwin, S., 2013. Spectral/hp Element Methods for Computational Fluid Dynamics. Oxford University Press.

Karniadakis, G.E., Israeli, M., Orszag, S.A., 1991. High-order splitting methods for the incompressible Navier-Stokes equations. J. Comput. Phys. 97, 414–443.

Kiya, M., Tamura, H., Arie, M., 1980. Vortex shedding from a circular cylinder in moderate-Reynolds-number shear flow. J. Fluid Mech. 101, 721–735.

Lam, K., Lin, Y., Zou, L., Liu, Y., 2012. Numerical simulation of flows around two unyawed and yawed wavy cylinders in tandem arrangement. J. Fluid Struct. 28, 135–151.

Lucor, D., Karniadakis, G.E., 2003. Effects of oblique inflow in vortex-induced vibrations, Flow. Turbulence and Combustion 71, 375–389.

Miliou, A., De Vecchi, A., Sherwin, S., Graham, J., 2007. Wake dynamics of external flow past a curved circular cylinder with the free stream aligned with the plane of curvature. J. Fluid Mech. 592, 89–115.
Miliou, A., Sherwin, S.J., Graham, J.M.R., 2003. Wake topology of curved cylinders at low Reynolds numbers, Flow. Turbulence and Combustion 71, 147–160.
Mittal, S., Kumar, V., Raghuvanshi, A., 1997. Unsteady incompressible flows past two cylinders in tandem and staggered arrangements. Int. J. Numer. Meth. Fluid. 25, 1315–1344.
Sumner, D., Price, S., Paidoussis, M., 2000. Flow-pattern identification for two staggered circular cylinders in cross-flow. J. Fluid Mech. 411, 263–303.
Sumner, D., Richards, M., Akosile, O., 2008. Strouhal number data for two staggered circular cylinders. J. Wind Eng. Ind. Aerod. 96, 859–871.
Thapa, J., Zhao, M., Cheng, L., Zhou, T., 2015. Three-dimensional flow around two circular cylinders of different diameters in a close proximity. Phys. Fluids 27, 085106.
Wilkins, S.J., Hogan, J.D., Hall, J.W., 2013. Vortex shedding in a tandem circular cylinder system with a yawed downstream cylinder. J. Fluid Eng. 135, 071202.
Williamson, C.H., 1996. Vortex dynamics in the cylinder wake. Annu. Rev. Fluid Mech. 28, 477–539.
Yong, B., Qiang, B., 2005. Subsea Pipelines and Risers, vol. 536. Elsevier Science Ltd, Amsterdam, pp. 548.
Younis, M., Alam, M., Zhou, Y., 2016. Flow around two non-parallel tandem cylinders. Phys. Fluids 28, 125106.
Zhao, M., Cheng, L., Zhou, T., 2009. Direct numerical simulation of three-dimensional flow past a yawed circular cylinder of infinite length. J. Fluid Struct. 25, 831–847.
Zhao, M., Thapa, J., Cheng, L., Zhou, T., 2013. Three-dimensional transition of vortex shedding flow around a circular cylinder at right and oblique attacks. Phys. Fluids 25, 014105.